# Microstructure evolution induced by the intrinsic heat treatment occurring during wire-arc additive manufacturing of an Al-Mg-Zn-Cu crossover alloy

Thomas Klein[1,*], Gloria Graf[2], Peter Staron[3], Andreas Stark[3], Helmut Clemens[2], Petra Spoerk-Erdely[2]

[1] LKR Light Metals Technologies Ranshofen, Austrian Institute of Technology, 5282 Ranshofen, Austria.

[2] Department of Materials Science, Montanuniversität Leoben, 8700 Leoben, Austria.

[3] Helmholtz-Zentrum Hereon, Institute of Materials Physics, 21502 Geesthacht, Germany.

[*] Corresponding author: thomas.klein@ait.ac.at

## Abstract

The implementation of wire-arc additive manufacturing for fabricating complex structures requires detailed knowledge of process-structure-property relationships. Results of scanning electron microscopy, wide-angle X-ray scattering, small-angle X-ray scattering, and microhardness measurements are presented to identify the mechanisms that govern the microstructure formation of an Al-Mg-Zn-Cu crossover alloy during wire-arc additive manufacturing. These analyses provide evidence on the formation of Mg-, Zn- and Cu-rich phases on different length scales spanning from ~10 µm (microsegregations), down to a few nm (bulk) following the intrinsic heat treatment. Future alloy concepts should build on the presented findings.

## Keywords

Wire-arc additive manufacturing (WAAM); Aluminum alloys; Intrinsic heat treatment; Microstructure evolution; Synchrotron radiation

## 1. Introduction

Wire-arc additive manufacturing (WAAM) has attracted great academic and industrial interest in recent years because of its advantages in terms of high deposition rates, large component sizes, high material efficiency, combined with relatively low facility investment costs [1]. For the extensive application of such a new process technology, the knowledge of sound process-structure-property relationships for each processed material is crucial. These correlations are, however, not yet established for WAAM as a result of the complex and unique process-intrinsic heat treatment (IHT) [2,3] and the large number of variable processing parameters. The IHT is characterized by fast solidification ensued by repetitive reheating and rapid cooling segments. These, in turn, lead to complex phase nucleation and growth sequences, which ultimately dominate the final material properties [4,5]. In case of age-hardenable aluminum alloys, the IHT entails the nucleation and coarsening of precipitates [4]. Intimate knowledge of the microstructural evolution at different length scales is, thus, required to exercise control over these complex reactions.

Here, we present recent findings on the IHT-induced microstructure evolution of a novel Al-Mg-Zn-Cu crossover alloy. Crossover Al-Mg-Zn-Cu alloys combine the high-strength of 7xxx alloys with the versatility of 5xxx alloys [6,7]. Moreover, the use of a single-alloy concept promises increased sustainability due to eases in recyclability [8]. Recent works have provided evidence for the good WAAM processability of the Al-5.5Mg-3.5Zn-0.3Cu alloy [9,10]. The research presented here significantly contributes to the understanding of the microstructural evolution of Al-Mg-Zn-Cu alloys subjected to the IHT of WAAM. Specifically, it provides necessary information on how to guide the thermal management and control upon WAAM deposition as well as on alloy development strategies. The results were obtained by means of scanning electron microscopy (SEM), wide-angle X-ray scattering (WAXS) and small-angle X-ray scattering (SAXS), as the observed reactions take place on different length scales and correlated to microhardness measurements.

## 2. Methods

The chemical composition of the investigated alloy wire and the deposit as determined by optical emission spectroscopy (SPECTROMAXx 6, SPECTRO Analytical Instruments) is given in Table 1. The composition of the deposit shows reduced concentrations of Mg and Zn – a result of the preferential evaporation of volatile chemical species in agreement with Refs. [9–12]. The wires were fabricated by means of vertical continuous casting of pre-material. Following the machining of cylindrical billets, the wires were hot extruded to a final diameter

of 1.6 mm. Details of the WAAM deposition procedure including the experimental setup can be found in the supplementary data. The IHT was characterized using a type-K thermocouple placed inside the melt pool and subsequently covered by the deposit [13].

SEM was performed using a Mira 3 microscope (Tescan) at 20 kV in back-scattered electron (BSE) mode on metallographic specimens polished with colloidal silica. Energy dispersive X-ray spectroscopy (EDX) was carried out using the EDAX Octane Elect system and the APEX software.

The in-situ WAXS and SAXS experiments were performed at the P07 high-energy materials science (HEMS) beamline operated by Hereon at PETRA III at the Deutsches Elektronen-Synchrotron (DESY) in Hamburg, Germany [14]. A dilatometer was used for simulating the IHT cycles [15]. Both WAXS and SAXS experiments were conducted simultaneously using two Perkin Elmer XRD 1621 flat panel detectors with a pixel size of 200 µm. The mean photon energy equaled 70 keV. The setups were calibrated using glassy carbon and silver behenate in the case of SAXS and a $LaB_6$ powder standard for WAXS. Detector images were azimuthally integrated with the aid of the software Fit2D [16]. The integrated intensity Q can be calculated according to Eq. (1):

$$Q = 4\pi \int_{q_{min}=0}^{q_{max}=\infty} \frac{d\Sigma}{d\Omega}(q) q^2 dq. \quad (1)$$

Since the macroscopic differential scattering cross-section $d\Sigma/d\Omega$ was integrated within a scattering vector $q$ range of 0.1 to 0.5 $nm^{-1}$, the integrated intensity is henceforth referred to as $Q'$. Particle volume fractions were determined with the software SANSfit [17,18], assuming a scattering contrast of $8.74 \times 10^{10}$ $cm^{-2}$.

Local mechanical properties were evaluated by Vickers microhardness measurements with a 0.1 kg load. Values given correspond to mean values of three indents, and the error corresponds to the standard deviation of the mean.

## 3. Results and discussion

Figure 1(a) exemplarily visualizes the temperature profile of the IHT. Peak and mean temperatures converge against values of ~230 °C and ~200 °C, respectively. These values were used to guide the thermal profile simulated for the scattering experiments. The inset in Fig. 1(a) shows the heating and cooling sequence of the second layer, where temperatures above the liquidus temperature of 625 °C are reached. Average cooling rates of ~50 K/s are observed in agreement with complementarily determined values [19]. The actual IHT depends on various

parameters including part geometry, measurement location and WAAM processing parameters. In Figs. 1(b) and (c) the microstructures formed in the 20$^{th}$ and the 1$^{st}$ layer are shown. Microsegregations of Mg, Zn and Cu (see EDX maps), which were induced by the solidification and now exhibit characteristic dimensions of <10 µm, remain similar during the IHT. However, the formation of a precipitate structure with dimensions of <250 nm is discernible along grain boundaries after repetitive reheating, see insets in Fig. 1(c). The chemical composition of the α-Al-grains' interiors determined by EDX amounts to Al-(5.00±0.21)Mg-(2.14±0.05)Zn-(0.19±0.04)Cu mass percent. The formation of a grain boundary decoration after repetitive reheating results from increased kinetics of phase formation in the vicinity of grain boundaries due to (i) the dependences of the nucleation rate and the growth rate on the supersaturation (see e.g. Robson [20]), which might be increased due to segregation effects, and (ii) the increased grain boundary diffusivity (see e.g. de Haas and de Hosson [21]).

Figure 2 shows the results of the in-situ synchrotron experiment under simulated IHT conditions (according to Fig. 2(c)). The WAXS signal, Fig. 2(a), evidences increasing T-phase diffraction peaks within the α-Al matrix on increasing aging duration in agreement with Refs. [6,10]. Figure 2(b) – (d) summarizes the results of the SAXS experiment. Clearly, an increasing scattering intensity is discernible (Fig. 2(b) and (c)), suggesting the formation of fine precipitates during the isothermal artificial aging procedure. In their early stages, the precipitates cover a size range well below 100 nm that SAXS is typically sensitive to. In the applied experimental setup, phases larger than 100 nm may contribute only with a $q^{-4}$ slope within the probed $q$ range. Thus, microsegregation zones and grain boundary precipitates are excluded from this analysis. The corresponding volume fractions of the nm-scaled particles have been evaluated quantitatively and depicted in Fig. 2(d). The observed particle fractions explicitly increase during the simulated IHT. Yet, they fall significantly below thermodynamic predictions [10], underpinning the previous observation that coarser phases, which cannot be probed by means of SAXS based on the set $q$ range, are already present after solidification and prior to the isothermal segment.

In the 1$^{st}$ and 20$^{th}$ layers, the microhardness amounts to 109±2 HV and 101±3 HV, respectively. It is assumed that in the topmost layer the material's hardness is dominated by the alloying elements, most importantly Mg and Zn, in solid solution. In subsequent layers, the IHT favors precipitation reactions. As the precipitates, however, take up an unfavorable size distribution (see Figs. 1 and 2), these reactions result in material softening. Similar effects have been argued to prevail during WAAM of an aluminum 7055 alloy [4], where general over-aging of the

precipitate structure was reported, but no discrepancies between grain boundaries and grain interior were presented.

## 4. Conclusions

A set of microstructural analyses was used to investigate the formation of second phases in an Al-Mg-Zn-Cu crossover alloy following the IHT of WAAM. Figure 3 schematically illustrates the prevailing phase distributions and size ranges of Mg-, Zn- and Cu-rich phases formed. Upon solidification, microsegregations develop with a typical size of <10 µm. This is due to the enrichment of the strongly segregating elements Mg, Zn and Cu in the interdendritic regions ahead of the solidification front. Their fine scale is related to the high cooling rates. However, a substantial amount of Mg, Zn and Cu remains in solid solution within the grains' interior, resulting in the formation of two populations of T-precipitates during the IHT, which precipitate either at grain boundaries (<250 nm) or as nm-scaled precipitates in the bulk. These results suggest that the microstructure formation of an Al-Mg-Zn-Cu alloy is complex and difficult to control. The variations between $1^{st}$ and $20^{th}$ layer additionally provide evidence for the discrepancies in the microstructure evolution between (single path) welding and WAAM. Future alloy development strategies need to incorporate the outlined aspects in their material/wire design for WAAM specifically.

**Acknowledgments**

This research was funded within the AIT's strategic research portfolio 2021. We acknowledge DESY (Hamburg, Germany), a member of the Helmholtz Association HGF, for the provision of experimental facilities. Parts of this research were carried out at PETRA III at beamline P07 (HEMS), operated by Helmholtz-Zentrum Hereon, and we would like to thank Dr. Norbert Schell and Dr. Emad Maawad for assistance in using the beamline and the dilatometer. Beamtime was allocated for proposal I-20190932 EC. The research leading to this result has been supported by the project CALIPSOplus under the Grant Agreement 730872 from the EU Framework Programme for Research and Innovation HORIZON 2020.

**References**

[1] B. Wu, Z. Pan, D. Ding, D. Cuiuri, H. Li, J. Xu, J. Norrish, J. Manuf. Process. 35 (2018) 127–139.

[2] K. Oyama, S. Diplas, M. M'hamdi, A.E. Gunnæs, A.S. Azar, Addit. Manuf. 26 (2019) 180–192.

[3] E. Aldalur, F. Veiga, A. Suárez, J. Bilbao, A. Lamikiz, J. Manuf. Process. 58 (2020) 615–626.

[4] B. Dong, X. Cai, S. Lin, X. Li, C. Fan, C. Yang, H. Sun, Addit. Manuf. 36 (2020) 101447.

[5] P. Kürnsteiner, P. Bajaj, A. Gupta, M.B. Wilms, A. Weisheit, X. Li, C. Leinenbach, B. Gault, E.A. Jägle, D. Raabe, Addit. Manuf. 32 (2020) 100910.

[6] L. Stemper, B. Mitas, T. Kremmer, S. Otterbach, P.J. Uggowitzer, S. Pogatscher, Mater. Des. 181 (2019) 107927.

[7] L. Stemper, M.A. Tunes, P. Oberhauser, P.J. Uggowitzer, S. Pogatscher, Acta Mater. 195 (2020) 541–554.

[8] D. Raabe, C.C. Tasan, E.A. Olivetti, Nature 575 (2019) 64–74.

[9] P. Morais, B. Gomes, P. Santos, M. Gomes, R. Gradinger, M. Schnall, S. Bozorgi, T. Klein, D. Fleischhacker, P. Warzcok, A. Falahati, E. Kozeschnik, Materials (Basel). 13 (2020) 1610.

[10] T. Klein, M. Schnall, B. Gomes, P. Warczok, D. Fleischhacker, P.J. Morais, Addit. Manuf. 37 (2021) 101663.

[11] T. Klein, M. Schnall, Int. J. Adv. Manuf. Technol. 108 (2020) 235–244.

[12] T. Yuan, Z. Yu, S. Chen, M. Xu, X. Jiang, J. Manuf. Process. 49 (2020) 456–462.

[13] A. Ho, H. Zhao, J.W. Fellowes, F. Martina, A.E. Davis, P.B. Prangnell, Acta Mater. 166 (2019) 306–323.

[14] N. Schell, A. King, F. Beckmann, T. Fischer, M. Müller, A. Schreyer, Mater. Sci. Forum

571–572 (2008) 261–266.

[15] P. Staron, T. Fischer, T. Lippmann, A. Stark, S. Danshpour, D. Schnubel, E. Uhlmann, R. Gerstenberger, B. Camin, W. Reimers, E. Eidenberger, H. Clemens, N. Huber, A. Schreyer, Adv. Eng. Mater. 13 (2011) 658.

[16] A.. Hammersley, S.O. Svensson, M. Hanfland, A.N. Fitch, D. Hausermann, High Press. Res. 14 (1996) 235–248.

[17] P. Staron, U. Christoph, F. Appel, H. Clemens, Appl. Phys. A Mater. Sci. Process. 74 (2002) 1163–1165.

[18] J.F. dos Santos, P. Staron, T. Fischer, J.D. Robson, A. Kostka, P. Colegrove, H. Wang, J. Hilgert, L. Bergmann, L.L. Hütsch, N. Huber, A. Schreyer, Acta Mater. 148 (2018) 163–172.

[19] T. Klein, A. Birgmann, M. Schnall, in: MATEC Web Conf., 2020, p. 01003.

[20] J.D. Robson, Acta Mater. 52 (2004) 4669–4676.

[21] M. de Haas, J.T.M. de Hosson, Scr. Mater. 44 (2001) 281–286.

## Tables

Table 1. Chemical composition of the aluminum crossover alloy in mass percent.

| | Al | Mg | Zn | Mn | Cu | Si | Fe | Zr |
|---|---|---|---|---|---|---|---|---|
| Wire | bal. | 5.9 | 3.6 | 0.5 | 0.3 | 0.1 | 0.1 | 0.1 |
| Deposit | bal. | 5.3 | 3.4 | 0.5 | 0.3 | 0.1 | 0.1 | 0.1 |

## Figures

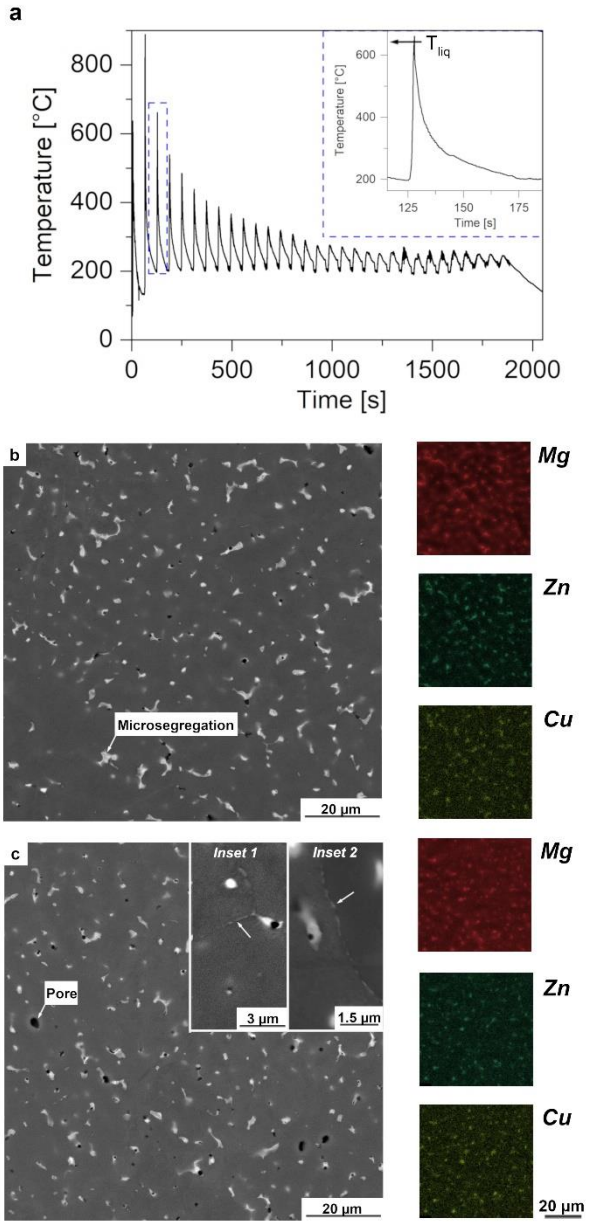


Fig. 1. (a) Exemplary measurement of the temperature profile (IHT). $T_{Liq}$: liquidus temperature of the alloy; (b) and (c) SEM micrographs with EDX maps of the major alloying elements of layers 20 (b) and 1 (c), respectively. The insets in (c) show the decoration of grain boundaries with precipitates.

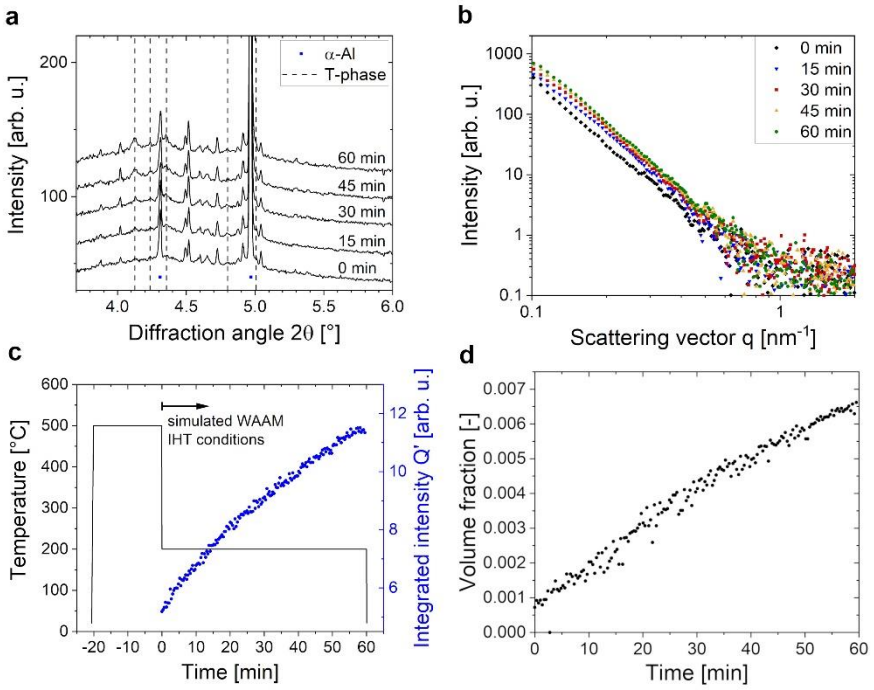


Fig. 2. Results of the in-situ diffraction and scattering experiments during 60 min of isothermal aging. (a) Selected integrated intensity vs. 2$\theta$ diffractograms (based on WAXS); (b) Selected scattering curves after azimuthal integration (based on SAXS); (c) Heat treatment profile used for the simulation of the IHT and evolution of the integrated intensity $Q$' during the IHT (based on SAXS); (d) Volume fraction evolution of fine precipitates (based on SAXS).

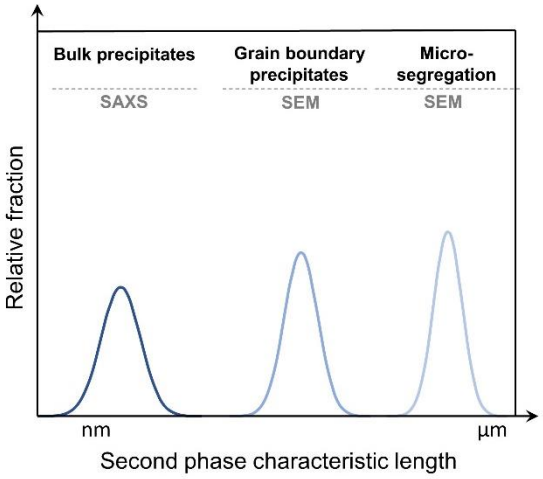


Fig. 3. Schematic illustration of the relative fractions of the IHT-induced phases with respect to the corresponding characteristic length.